Deshielding Anions Enable Solvation Chemistry Control of $LiPF_6$-based Electrolyte towards Low-Temperature Lithium-ion Batteries

Song Yuan, Shengkai Cao, Xi Chen, Jiaqi Wei, Zhisheng Lv, Huarong Xia, Jiaofu Li, Hang Zhang, Lin Liu, Changhao Tian, Lixun Chen, Wei Zhang, Zhenxiang Xing, Haicheng Li, Shuzhou Li, Qiang Zhu, Xue Feng* and Xiaodong Chen**

Mr. S. Yuan, Mr. X. Chen, Mr. L. Chen
Institute of Flexible Electronics Technology of THU, Tsinghua University, Jiaxing, Zhejiang 314000, People's Republic of China.

Mr. S. Yuan, Mr. X. Chen, Dr. J. Wei, Dr. H. Xia, Dr. J. Li, Dr. H. Zhang, Dr. L. Liu, Mr. C. Tian, Mr. L. Chen, Dr. W. Zhang, Prof. S. Li, Prof. X. Chen
Innovative Centre for Flexible Devices (iFLEX), Max Planck–NTU Joint Lab for Artificial Senses, School of Materials Science and Engineering, Nanyang Technological University, 50 Nanyang Avenue, 639798, Republic of Singapore.
E-mail: chenxd@ntu.edu.sg

Dr. S. Cao, Dr. Z. Lv, Mr. C. Tian, Mr. Z. Xing, Prof. Q. Zhu
Institute of Materials Research and Engineering (IMRE), Agency for Science, Technology and Research (A*STAR), 2 Fusionopolis Way, Innovis #08-03, Singapore 138634, Republic of Singapore.
E-mail: zhuq@imre.a-star.edu.sg

Dr. H. Li, Prof. X. Feng
Center for Flexible Electronics Technology, Tsinghua University, No. 30, Shuangqing Road, Beijing 100084, People's Republic of China.
E-mail: fengxue@tsinghua.edu.cn

Keywords: Deshielding anions, $LiPF_6$-based electrolyte, Solvation design, Low temperature, Lithium-ion batteries.

Abstract

Severe capacity decay under subzero temperatures remains a significant challenge for lithium-ion batteries (LIBs) due to the sluggish interfacial kinetics. Current efforts to mitigate this deteriorating interfacial behavior rely on high-solubility lithium salts (e.g., Lithium bis(trifluoromethanesulfonyl)imide (LiTFSI), Lithium bis(fluorosulfonyl)imide (LiFSI))-based electrolytes to construct anion participated solvation structures. However, such electrolytes bring issues of corrosion on the current collector and increased costs. Herein, we utilized the most commonly used Lithium hexafluorophosphate ($LiPF_6$) instead, to establish a peculiar solvation structure with a high ratio of ion pairs and aggregates by introducing a deshielding NO_3^- additive for low-temperature LIBs. The deshielding anion significantly reduces the energy barrier for interfacial behavior at low temperatures. Benefiting from this, the graphite (Gr) anode retains a high capacity of ≈ 72.3% at −20 ℃, which is far superior to the 32.3% and 19.4% capacity retention of counterpart electrolytes. Moreover, the $LiCoO_2$/Gr full cell exhibits a stable cycling performance of 100 cycles at −20 ℃ due to the inhibited lithium plating. This work heralds a new paradigm in $LiPF_6$-based electrolyte design for LIBs operating at subzero temperatures.

1. Introduction

Lithium-ion batteries (LIBs) are the predominant power source for nearly all contemporary portable devices and electric vehicles, and their ubiquity is steadily increasing.[1] Nevertheless, significant capacity decay in LIBs at low temperatures poses a major obstacle to their broader application in aerospace, deep-sea explorations, and electrical vehicles operating in cold areas.[2] Although the rate of all electrochemical steps decreases at subzero temperatures, the dominant factor contributing to this low-capacity retention is the sluggish charge transfer process, also known as the desolvation process.[3] Current efforts mainly focus on regulating solvation structures of the electrolyte by super-concentrated strategies or the use of weak polar solvents.[4] These approaches involve introducing anions to reduce the polar solvent in the solvation structure, thereby achieving a fast desolvation process. However, all these modification strategies face limitation when applied to the commonly used Lithium hexafluorophosphate ($LiPF_6$)-based electrolytes due to their solubility constraints. They rely on highly soluble lithium salts (e.g., Lithium bis(trifluoromethanesulfonyl)imide (LiTFSI), Lithium bis(fluorosulfonyl)imide (LiFSI)) with high cost. In addition, these salts suffer from the intrinsic issue of corrosion on the aluminium current collector and are not the ideal candidates of the lithium salt for commercialized LIBs.[5] Therefore, a strategy to regulate the solvation sheath of commonly used $LiPF_6$ electrolytes towards low-temperature applications is highly demanded though remains challenging.

To achieve this goal, we delved into the low-temperature electrolyte design for the sluggish charge transfer process and the predicament of using $LiPF_6$ as the lithium salt. The charge transfer process represents the movement of solvated lithium ions into the electrodes and it has been proved that the desolvation process contributed to the main charge transfer resistance (R_{ct}).[6] The change of R_{ct} with temperature can be depicted by (eq 1),

$$\frac{1}{R_{ct}} = A_0 e^{-E_a/RT} \quad (1)$$

Where A_0 is the pre-exponential constant, E_a means the activation energy, R represents the gas constant and T corresponds to the absolute temperature.[3a] Therefore, the goal of solvation sheath design is to decrease the energy barrier (E_a) required for removing polar solvent from lithium ions, mitigating the rapid increase of R_{ct} at low temperature (Figure 1a). The key to achieving this is to replace the solvent in the first solvation sheath with anions because the desolvation process of anions themselves is much easier due to the Coulombic repulsive force.[7] However, due to the poor dissociation ability of $LiPF_6$, it cannot introduce PF_6^- anions into the solvation sheath by forming a super-concentrated electrolyte (> 4 M) or dissolving in a weak polar solvent.[8] As a potential solution to circumvent the intrinsic limitations of $LiPF_6$, introducing deshielding anions to the electrolyte is proposed (Figure 1b, c). The deshielding effect will reduce the influence of polar solvent on Li^+ due to the high affinity of the introduced anion with Li^+. Consequently, the deshielding anion will effectively displace part polar solvent molecules within the solvation structure at a low concentration. Besides, the formed anion-participated solvation sheath will enable the whole electrolyte system compatible with graphite anodes by forming a densely anion-derived solid electrolyte interface (SEI). Accordingly, the reduced energy barrier for the charge transfer process would accelerate the intercalation kinetics and avoid safety issues induced by lithium plating (Figure 1d).

Herein, we demonstrate that the anion-participated solvation sheath in $LiPF_6$-based electrolytes can be achieved by introducing a deshielding anion while maintaining the low electrolyte concentration, thereby enhancing the low-temperature performance of LIBs. Nitrate anion (NO_3^-) was screened from a series of anions as the deshielding anion by the nuclear magnetic resonance (NMR) and cyclic voltammetry (CV). Raman spectrum and molecular dynamic (MD) simulation confirm the high ratio of ion pairs and aggregates in electrolyte microstructure.

Accordingly, the fast increase of charge transfer resistance at low temperatures was greatly inhibited and the graphite anodes were endowed with a high-capacity retention of ≈ 72.3% at −20 °C, much higher than counterpart electrolytes (32.3% and 19.4%). The superior low-temperature performance was further demonstrated in $LiCoO_2$/Gr full cell and the time-of-flight secondary ion mass spectrometry (ToF-SIMS) confirmed the inhibited lithium plating. This study brings back the use of common lithium salts by adding a deshielding anion to facilitate an anion-involved solvation sheath for low-temperature LIBs.

2. Results and Discussion

The core of $LiPF_6$-based electrolyte design is to select the proper deshielding anion that can enter the first solvation sheath with low concentration. Here, NMR spectroscopy was implemented to evaluate the ability of introduced anions to coordinate Li^+. The entry of anions into the solvation sheath would squeeze out the polar solvent and reduce their shielding effect, leading to the ^{7}Li peak shift towards the higher value.[9] Based on the selected result (Figure 2a, Figure S1, Supporting Information), inorganic ions such as NO_3^-, Cl^-, and Br^-, exhibit a stronger coordinating ability to Li^+. As the introduced lithium salt also requires a high dissociation ability of solvent, ether molecules were chosen to replace traditional carbonate-based solvents which show almost no solubility to these inorganic lithium salts.[10] However, the change of the main solvent to dimethoxyethane (DME) inevitably incurs incompatible issues with graphite anodes, resulting in co-intercalation of the solvent and a consequent capacity reduction.[11] To address this problem, the regular film-forming co-solvent fluoroethylene carbonate (FEC) was mixed with DME as a ratio of 3:7, denoted as D7F3, to prevent solvent co-intercalation through SEI formation in the first cycle. However, even though the FEC was decomposed at 1.18 V as expected, the co-intercalation (0.61 V) still occurred in the first cycle and lead to a lower initial Coulombic efficiency of 65.6%, indicating the incompatibility of D7F3 with graphite anodes in the first cycle (Figure 2b, Figure S2,

Supporting Information). Consequently, the second selection criteria mandate the introduced anions to prevent the co-intercalation of ether molecules. Based on the CV tests of various anions, five potential candidates, including BOB^-, BF_4^-, $DFOB^-$, F^- and NO_3^- were identified as shown in Figure S3. Notably, these anions successfully prevented solvent co-intercalation peaks from emerging and shows a higher initial Coulombic efficiency (77.4% for NO_3^-) due to the formation of an anion-derived solid electrolyte interphase (SEI) before FEC decomposition. In contrast, all other test anions failed to help build a dense SEI, and corresponding co-intercalation peaks remained visible (Figure S4, Supporting Information). Based on the two requirements of deshielding ability to polar solvent in the solvation sheath and the prevention of solvent co-intercalation, NO_3^- was selected as the deshielding anion for proof of the concept and the corresponding electrolyte is noted as D7F3N (Figure 2a). Notably, the chosen solvent combination and $LiNO_3$ are usually used in lithium metal battery.[12] However, their application in LIBs has been hindered by compatibility issues with graphite anodes and negligible solubility of $LiNO_3$ in commonly used carbonate solvent. Through our rational design, for the first time, this solvent combination and $LiNO_3$ can be used to modulate the solvation structure of $LiPF_6$-based electrolytes towards low-temperature operation of LIBs. Raman spectroscopy and MD simulations were also used to detect the influence of NO_3^- on solvation structures. The signals of free anions (FA, 1037.0 cm^{-1}, non-coordinated NO_3^-,) contact ion pair (CIP, 1042.0 cm^{-1} NO_3^- binding with one Li^+) and ion aggregate (AGG, 1052.0 cm^{-1}, one NO_3^- binding with multiple Li^+) were captured in the D7F3N electrolyte, indicating the entry of NO_3^- into the solvation sheath (Figure 2c).[13] Additionally, the results of MD simulations exhibit a pronounced inverse relationship between the quantity of DME molecules and the presence of NO_3^- within the solvation sheath. Specifically, a substantial presence of NO_3^- corresponds to a lower quantity of DME molecules (Figure 2d, Figure S5, Supporting Information). Besides, the radial distribution function (RDF) derived from MD simulation confirms that nearly all NO_3^- come into the primary solvation structure (Figure 2e), which is well aligned with the results

obtained from Raman spectroscopy. In contrast with the anion-participated solvation structure in D7F3N, PF_6^- remain separated by solvent molecules in D7F3 electrolytes due to their limited affinity to Li^+. To find the optimal concentration of introduced NO_3^-, NMR was used to detect the ^7Li shift at various concentrations and 0.4 M was found to exhibit the strongest deshielding effect (Figure S6, Supporting Information). All these results demonstrate that the deshielding anion successfully constructs the anion-participating solvation structure in the $LiPF_6$-based electrolyte and maintains good compatibility with graphite anodes.

To further understand the role of deshielding anions on passivating graphite anodes and constructing conductive interface, a combination of transmission electron microscopy (TEM) and X-ray photoelectron microscopy (XPS) were used to characterize the SEI. As shown in Figure 3a, the thickness of the SEI layer on the graphite anode after 10 cycles in D7F3N is only approximately 2.01 nm, whereas those formed in D7F3 and LP40 (The commercial 1.0 M $LiPF_6$ in EC: DEC=1:1) are non-uniform and exhibit a greater thickness of 19.32 nm and 5.84-12.71 nm (Figure 3b, c), respectively. This morphology difference suggests that the SEI decomposed from NO_3^- is denser and more stable to inhibit continuous growth of the SEI layer and this thinner structure will lead to a faster Li^+ transportation. [4e, 14] To further identify the spatial compositional difference of the SEI layer in three electrolytes, in-depth XPS characterization was conducted on three electrolytes by Ar^+ sputtering. The top surface of the cycled graphite anode in D7F3N exhibited a lower content of organic components (Li_2CO_3/$ROCO_2Li$ 55.5 eV) than D7F3 and LP40 (Figure 3d, Figure S7 and S8, Supporting Information), indicating the inhibited decomposition of organic solvent in the NO_3^- modified solvation structure. Moreover, among these inorganic components, besides the commonly observed conductive component (LiF, 56.4 eV) in graphite's SEI, the presence of LiN_3 (55.9 eV) was detected only in the SEI formed in D7F3N (Figure 3d, Figure S9, Supporting Information), which is known to be a conductive component in the SEI of lithium metal anodes.[15] As shown in Figure 3e, with the

increase of sputtering time from 0 to 8 min, the content of conductive components in D7F3 and LP40 remains at a lower level with minimal fluctuations. However, the proportion of total conductive parts continues to increase beyond 45% in D7F3N and the LiF was replaced with LiN_3 as the primary conductive inorganic part. The dominance of LiN_3 as the primary conductive part in the inner structure of SEI indicates that NO_3^- in solvation sheath prefers to decompose at the early stage of SEI formation. The resulting densely electronic insulated interface prevents further fast growth of the SEI and solvent co-intercalation. All these prove that the anion-participated solvation chemistry greatly influences the SEI formation, resulting in an anion-derived SEI component in D7F3N and the solvent-derived interface in D7F3 and LP40.

As conventional approaches to mitigate capacity decay in subzero environments depend heavily on warming systems, we measured both the charging and discharging process at low temperatures to avoid extra energy consumption (Figure S10, Supporting Information). The key to achieving low-temperature cycling lies in the graphite anodes due to their sluggish Li^+ intercalation kinetics and the corresponding occurrence of lithium plating (Figure S11, Supporting Information). Therefore, the kinetic processes of artificial graphite anodes in various electrolytes were strictly evaluated by EIS (Figure S12 and S13, Supporting Information). However, it is quite challenging for the traditional method of merely fitting Nyquist plots to deconvolute four consecutive electrochemical steps: 1) Li^+ diffusion in the electrolyte, 2) Li^+ transport through the SEI, 3) charge transfer, and 4) Li^+ diffusion in the graphite, as some of these steps have similar time constants (τ), leading to the overlap of semicircles.[16] Therefore, the distribution of relaxation time (DRT) method was employed to analyze the EIS data, enabling more accurate modeling of EIS data and distinguishing between overlapping processes.[17] As shown in Figure S14, the EIS data of LP40 at room temperature can be decoupled into three peaks by the DRT method, corresponding to the process of diffusing

through SEI, charge transfer, and solid diffusion, respectively.[17] The change of resistance for each electrochemical step in three different electrolyte systems was investigated by continuously decreasing the temperature (Figure 4a). In the three electrolyte systems, each step became sluggish with a temperature decrease, resulting in resistance rise and the τ moves towards a high value. Similar to previous studies, R_{ct} is clear the rate-limiting step for the intercalation process of Li^+ into graphite anodes in three electrolytes when temperature continuously decreases to −20 ℃.[2] However, the τ of R_{ct} under low temperatures for D7F3N was one magnitude lower than that of D7F3 and LP40, indicating a faster charge transfer process. Moreover, with the temperature decrease from 20 ℃ to −20 ℃, the R_{ct} for LP40 and D7F3 exhibited a fast increase to 1531 and 1026 Ω, respectively, whereas D7F3N showed a mild rise to only 359 Ω, which was even close to the R_{ct} for LP40 at −5 ℃ (Figure 4b). Therefore, as expected from our electrolyte design principle, the energy barrier for the charge transfer process of D7F3N was greatly limited to 45.56 KJ/mol (Figure S15, Supporting Information), much lower than that of D7F3 (62.36 KJ/mol) and LP40 (63.18 KJ/mol), mitigating the fast increase of R_{ct} with temperature decrease. Moreover, to eliminate the effect of concentration increase after introducing additives, the change of interfacial resistance and energy barrier of desolvation for D7F3 with adding LiTFSI and $LiPF_6$ were also measured, respectively (Figure S16, Supporting Information). The derived activation energy (desolvation energy) shows negligible change compared to the D7F3, confirming the modified desolvation process is resulted from the introduced deshielding anions. Correspondingly, the low-temperature cycling test for graphite half-cells with three different electrolytes exhibited a significant difference in electrochemical performance. When continuously decreasing the temperature from 25, 0, −10 to −20 ℃, the graphite anodes in D7F3N kept a low-capacity decay below 30% whereas a fast decrease could be observed for D7F3 and LP40, which agrees with their fast increase in interfacial resistance, indicating the effect of NO_3^- on promoting interfacial kinetics (Figure 4c). Moreover, cycling tests at −20 ℃ revealed that D7F3N rendered much higher capacity retention

at various rates compared with the D7F3 and LP40 (Figure 4d, e). At 0.2 C, in contrast with a low capacity of around 50 mAh g^{-1} for control groups, the graphite anode in D7F3N delivered a high capacity of close to 200 mAh g^{-1} and kept stable for 200 cycles (Figure S17, Supporting Information). Besides the graphite anode, D7F3N is also compatible with silicon/carbon composite anode and exhibits a higher capacity retention at low temperature compared with the D7F3 (Figure S18, Supporting Information). To further confirm the improved electrochemical performance resulting from the introduced deshielding anions, a systematic study was conducted to eliminate the influence of other factors (e.g., solvent ratio, concentration change). As Figure S19 shown, the electrochemical performance exhibits a certain decrease with an increased FEC percentage (6:4). This decrease is attributed to the high melting point solvent (FEC), which elevates the melting point of the overall system. In contrast, the electrochemical performance shows a negligible change when decreasing the FEC ratio (8:2), indicating the minor effect of the solvent on the desolvation process once the melting point requirement is met. Moreover, the $TFSI^-$ and PF_6^-, which exhibited a negligible deshielding ability during NMR tests, were introduced into D7F3. In contrast with the NO_3^-, they produced a negligible effect on improving low-temperature performance, eliminating the influence from concentration change (Figure S20 and S21, Supporting Information). This high-capacity retention under subzero conditions is also competitive compared to previous low-temperature electrolyte design strategies which required highly soluble lithium salts but with intrinsic issue for commercialization (Table S1, Supporting Information). In addition, this impressive low-temperature cycling capability in D7F3N was achieved without sacrificing the room-temperature performance of the graphite anode. Figure S22 illustrates the rate capability and long cycling performance of graphite anodes in various electrolytes under room temperatures, wherein cycling Coulombic efficiencies remained consistently high (> 99%) across all groups. However, D7F3N demonstrates a higher reversible capacity of 331 mAh g^{-1} at 1 C, and the battery can maintain capacity retention of over 60% as the rate increases to 4 C, remaining

stable for up to 1000 cycles. On the other hand, commercial electrolyte LP40 exhibited a significant capacity decay, delivering only around 60 mAh g^{-1} at 4 C. Although the reduced capacity for D7F3 at high rates is less severe compared to LP40, the loss of capacity induced by co-intercalation of solvent at the first cycle make it a less competitive option. Moreover, to measure the electrochemical performance of graphite anodes across a broader temperature range, tests were conducted using various electrolytes under high temperatures (50 ℃). In D7F3N, the graphite anode demonstrated an impressive capacity of 324 mAh/g at 4 C under 50 ℃ and maintained stable cycling over 500 cycles (Figure S23, Supporting Information). Conversely, both D7F3 and LP40 exhibited limited capacity retention, with a rapid 50% capacity decay observed after 500 cycles under high temperatures. Based on the improved electrochemical performance and lower conductivity of D7F3N (Figure S24, Supporting Information), we demonstrate that the key for LIBs at subzero temperature is to solve the sluggish interfacial behavior and introduce deshielding anion to control solvation sheath is effective.

We further assembled full cells to evaluate the low-temperature performance of these electrolytes in both $LiCoO_2$/Gr and NCM811/Gr systems. In the case of the D7F3 electrolyte, a rapid capacity decay was observed after just 60 cycles, accompanied by a short-circuit-induced failure in the $LiCoO_2$/Gr system (Figure 5a). Meanwhile, when the D7F3 is employed in NCM811/Gr full cell, a sharp capacity decline happened from the initial stage and lead to battery failure within 40 cycles (Figure S25, Supporting Information). Conversely, the full cell utilizing the D7F3N electrolyte exhibited superior capacity retention and maintained stability over 100 and 200 cycles, respectively. At ultra-low temperatures (−40 ℃), the full cell using D7F3N delivers a remarkable three times higher capacity than D7F3 (Figure 5b). The assembled flexible pouch cell efficiently powers light-emitting diode (LED) lamps (Figure 5c), exhibiting its potential as a power source for flexible electronics in extreme conditions.[18] To

further explore the mechanism behind this cycling difference, a post-mortem analysis was conducted to evaluate the cycled graphite anode in different electrolytes. Time-of-flight secondary in mass spectrometry (ToF-SIMS) gives a distribution of lithium metal deposited on the graphite surface. The graphite surface in D7F3N exhibits a negligible lithium metal content in contrast with the severe lithium plating in D7F3 (Figure 5d, e, Figure S26, Supporting Information). As depicted in depth profile (Figure S27, Supporting Information), the intensity of Li^- for D7F3 is significantly higher than that in D7F3N, exhibiting a stable content within 150 nm, indicative of the presence of plated lithium metal. In contrast, a much lower content of Li^- signal and a distinct drop at a depth of 20 nm, attributable to the solid electrolyte interphase (SEI), are observed in D7F3N. As the characterized graphite anodes are all in the discharge state, the lithium metal plated in D7F3 belongs to 'dead lithium', leading to irreversible capacity loss.

3. Conclusion

In conclusion, we demonstrated that the deshielding anion, which successfully regulates the solvation chemistry of $LiPF_6$-based electrolyte at a low concentration, can effectively mitigate the fast increase in charge transfer resistance of LIBs at subzero temperatures, using NO_3^- as a concept proof. Further electrolyte characterization and interfacial kinetics measurement indicated that the solvation structure with a high ratio of ion pairs and aggregates formed and the energy barrier of charge transfer resistance was greatly reduced. Benefiting from this, the cycling performance of graphite anodes achieves a high capacity retention of 78 % under −20 ℃, compared to 32.3 % of the electrolytes without deshielding introduction. Meanwhile, the full cell tests also sustain a stable cycling performance with inhibited lithium plating at −20 ℃ and show the available operation under a lower temperature of −40 ℃. Our deshielding anion strategy provides an effective approach to regulate the solvation chemistry of $LiPF_6$-based low-

temperature electrolytes, extending the potential applications of this most commercially successful lithium salt to a wider range of fields for next-generation LIBs.

4. Experimental Section/Methods

The detailed experimental process is available in the Supporting Information.

Supporting Information

Supporting Information is available from the Wiley Online Library or from the author.

Acknowledgements

Yuan Song acknowledges the research scholarship awarded by the Institute of Flexible Electronics Technology of Tsinghua, Zhejiang (IFET-THU), Nanyang Technological University (NTU), and Qiantang Science and Technology Innovation Center, China (QSTIC). The project was supported by the National Research Foundation (NRF), Prime Minister's Office, Singapore, under the Singapore Hybrid-Integrated Next-Generation μ-Electronics (SHINE) Centre.

Received: ((will be filled in by the editorial staff))

Revised: ((will be filled in by the editorial staff))

Published online: ((will be filled in by the editorial staff))

References

[1] a) J. M. Tarascon, M. Armand, *Nature* **2001**, 414, 359; b) M. Li, J. Lu, Z. Chen, K. Amine, *Adv. Mater.* **2018**, 30, 1800561; c) H. Xia, W. Zhang, S. Cao, X. Chen, *ACS nano* **2022**, 16, 8525; d) S. Cao, Z. Zhu, W. Zhang, H. Xia, Y. Zeng, S. Yuan, X. Ge, Z. Lv, J. Wei, L. Liu, Y.

Du, S. Xi, X. j. Loh, X. Chen, *Adv. Mater.* **2023**, 2304900; e) X. Zeng, M. Li, D. A. El-Hady, W. Alshitari, A. S. Al-Bogami, J. Lu, K. Amine, *Adv. Energy Mater.* **2019**, 9, 1900161.

[2] a) A. Gupta, A. Manthiram, *Adv. Energy Mater.* **2020**, 10, 2001972; b) D. Hubble, D. E. Brown, Y. Zhao, C. Fang, J. Lau, B. D. McCloskey, G. Liu, *Energy Environ. Sci.* **2022**, 15, 550; c) N. Zhang, T. Deng, S. Zhang, C. Wang, L. Chen, C. Wang, X. Fan, *Adv. Mater.* **2022**, 34, 2107899; d) Y. Feng, L. Zhou, H. Ma, Z. Wu, Q. Zhao, H. Li, K. Zhang, J. Chen, *Energy Environ. Sci.* **2022**, 15, 1711; e) X. Ge, S. Cao, Z. Lv, Z. Zhu, Y. Tang, H. Xia, H. Zhang, J. Wei, W. Zhang, Y. Zhang, Y. Zeng, X. Chen, *Adv. Mater.* **2022**, 34, 2206797; f) W. Zhang, H. Xia, Z. Zhu, Z. Lv, S. Cao, J. Wei, Y. Luo, Y. Xiao, L. Liu, X. Chen, *CCS Chem.* **2021**, 3, 1245.

[3] a) W. Zhang, X. Sun, Y. Tang, H. Xia, Y. Zeng, L. Qiao, Z. Zhu, Z. Lv, Y. Zhang, X. Ge, S. Xi, Z. Wang, Y. Du, X. Chen, *J. Am. Chem. Soc.* **2019**, 141, 14038; b) Q. Li, D. Lu, J. Zheng, S. Jiao, L. Luo, C. M. Wang, K. Xu, J. G. Zhang, W. Xu, *ACS Appl. Mater. Interfaces* **2017**, 9, 42761; c) S. S. Zhang, K. Xu, T. R. Jow, *J. Power Sources.* **2003**, 115, 137; d) J. Holoubek, Y. Yin, M. Li, M. Yu, Y. S. Meng, P. Liu, Z. Chen, *Angew. Chem. Int. Ed.* **2019**, 58, 18892; e) J. Holoubek, H. Liu, Z. Wu, Y. Yin, X. Xing, G. Cai, S. Yu, H. Zhou, T. A. Pascal, Z. Chen, *Nat. Energy.* **2021**, 6, 303.

[4] a) L. L. Jiang, C. Yan, Y. X. Yao, W. Cai, J. Q. Huang, Q. Zhang, *Angew. Chem. Int. Ed.* **2021**, 60, 3402; b) Y. X. Yao, N. Yao, X. R. Zhou, Z. H. Li, X. Y. Yue, C. Yan, Q. Zhang, *Adv. Mater.* **2022**, 34, 2206448; c) J. Xu, J. Zhang, T. P. Pollard, Q. Li, S. Tan, S. Hou, H. Wan, F. Chen, H. He, E. Hu, K. Xu, X.-Q. Yang, O. Borodin, C. Wang, *Nature* **2023**, 614, 694; d) Y. Yang, Z. Fang, Y. Yin, Y. Cao, Y. Wang, X. Dong, Y. Xia, *Angew. Chem. Int. Ed.* **2022**, 134, e202208345; e) B. Nan, L. Chen, N. D. Rodrigo, O. Borodin, N. Piao, J. Xia, T. Pollard, S. Hou, J. Zhang, X. Ji, J. Xu, X. Zhang, L. Ma, X. He, S. Liu, H. Wan, E. Hu, W. Zhang, K. Xu, X.-Q. Yang, B. Lucht, C. Wang, *Angew. Chem. Int. Ed.* **2022**, 61, e202205967.

[5] a) L. Qiao, U. Oteo, M. Martinez-Ibañez, A. Santiago, R. Cid, E. Sanchez-Diez, E. Lobato, L. Meabe, M. Armand, H. Zhang, *Nat. Mater.* **2022**, 21, 455; b) A. Abouimrane, J. Ding, I.

Davidson, *J. Power Sources.* **2009**, 189, 693; c) G. Xu, X. Shangguan, S. Dong, X. Zhou, G. Cui, *Angew. Chem. Int. Ed.* **2020**, 59, 3400.

[6] K. Xu, A. von Cresce, U. Lee, *Langmuir* **2010**, 26, 11538.

[7] X. Fan, X. Ji, L. Chen, J. Chen, T. Deng, F. Han, J. Yue, N. Piao, R. Wang, X. Zhou, X. Xiao, L. Chen, C. Wang, *Nat. Energy.* **2019**, 4, 882.

[8] a) Y. Yamada, J. Wang, S. Ko, E. Watanabe, A. Yamada, *Nat. Energy.* **2019**, 4, 269; b) X. Cao, H. Jia, W. Xu, J.-G. Zhang, *J. Electrochem. Soc.* **2021**, 168, 010522.

[9] a) T. Ma, Y. Ni, Q. Wang, W. Zhang, S. Jin, S. Zheng, X. Yang, Y. Hou, Z. Tao, J. Chen, *Angew. Chem. Int. Ed.* **2022**, 134, e202207927; b) W. Wahyudi, V. Ladelta, L. Tsetseris, M. M. Alsabban, X. Guo, E. Yengel, H. Faber, B. Adilbekova, A. Seitkhan, A. H. Emwas, M. N.Hedhili, L.-J. Li, V. Tung, N. Hadjichristidis, T. D. Anthopoulos, J. Ming, *Adv. Funct. Mater.* **2021**, 31, 2101593.

[10] W. Zhang, Y. Lu, L. Wan, P. Zhou, Y. Xia, S. Yan, X. Chen, H. Zhou, H. Dong, K. Liu, *Nat. Commun.* **2022**, 13, 2029.

[11] a) L. L. Jiang, C. Yan, Y. X. Yao, W. Cai, J. Q. Huang, Q. Zhang, *Angew. Chem. Int. Ed.* **2021**, 60, 3402; b) H. Kim, K. Lim, G. Yoon, J. H. Park, K. Ku, H. D. Lim, Y. E. Sung, K. Kang, *Adv. Energy Mater.* **2017**, 7, 1700418; c) P. Ma, P. Mirmira, P. J. Eng, S.-B. Son, I. D. Bloom, A. S. Filatov, C. V. Amanchukwu, *Energy Environ. Sci.* **2022**, 15, 4823; d) B. Jache, J. O. Binder, T. Abe, P. Adelhelm, *Phys. Chem. Chem. Phys.* **2016**, 18, 14299.

[12] a) G. Huang, Y. Liao, X. Zhao, X. Jin, Z. Zhu, M. Guan, Y. Li, *Adv. Funct. Mater.* **2023**, 33, 2211364; b) G. Huang, G. Chen, X. Jin, K. Ge, M. Guan, Y. Li, *J. Power Sources* **2023**, 556, 232497; c) X. Q. Zhang, X. Chen, X. B. Cheng, B. Q. Li, X. Shen, C. Yan, J. Q. Huang, Q. Zhang, *Angew. Chem. Int. Ed.* **2018**, 57, 5301.

[13] a) T. Chen, Z. Jin, Y. Liu, X. Zhang, H. Wu, M. Li, W. Feng, Q. Zhang, C. Wang, *Angew. Chem. Int. Ed.* **2022**, 61, e202207645; b) Y. Liang, W. Wu, D. Li, H. Wu, C. Gao, Z. Chen, L. Ci, J. Zhang, *Adv. Energy Mater.* **2022**, 12, 2202493.

[14] a) M. S. Kim, Z. Zhang, P. E. Rudnicki, Z. Yu, J. Wang, H. Wang, S. T. Oyakhire, Y. Chen, S. C. Kim, W. Zhang, T. B. David, X. Kong, R. Xu, Z. Huang, W. Huang, S. F.Bent, L.-W. Wang, J. Qin, Z. Bao, Y. Cui, *Nat. Mater.* **2022**, 21, 445; b) C. Sun, X. Ji, S. Weng, R. Li, X. Huang, C. Zhu, X. Xiao, T. Deng, L. Fan, L. Chen, X. Wang, C. Wang, X. Fan, *Adv. Mater.* **2022**, 34, 2206020; c) Z. Zhu, Y. Tang, Z. Lv, J. Wei, Y. Zhang, R. Wang, W. Zhang, H. Xia, M. Ge, X. Chen, *Angew. Chem. Int. Ed.* **2018**, 130, 3718.

[15] a) S. Xiong, K. Xie, Y. Diao, X. Hong, *Electrochim. Acta.* **2012**, 83, 78; b) C. Yan, Y. X. Yao, X. Chen, X. B. Cheng, X. Q. Zhang, J. Q. Huang, Q. Zhang, *Angew. Chem. Int. Ed.* **2018**, 57, 14055; c) J. Fu, X. Ji, J. Chen, L. Chen, X. Fan, D. Mu, C. Wang, *Angew. Chem. Int. Ed.* **2020**, 132, 22378; d) Q. Shi, Y. Zhong, M. Wu, H. Wang, H. Wang, *Proc. Natl. Acad. Sci. U.S.A.* **2018**, 115, 5676.

[16] a) S. S. Zhang, K. Xu, T. Jow, *Electrochim. Acta.* **2006**, 51, 1636; b) S. Zhang, M. S. Ding, K. Xu, J. Allen, T. R. Jow, *Electrochem. Solid-State Lett* **2001**, 4, A206.

[17] a) X. Zhou, Z. Pan, X. Han, L. Lu, M. Ouyang, *J. Power Sources.* **2019**, 417, 188; b) X. Zhou, J. Huang, Z. Pan, M. Ouyang, *J. Power Sources.* **2019**, 426, 216; c) Y. Lu, C.-Z. Zhao, J.-Q. Huang, Q. Zhang, *Joule* **2022**, 6, 1172; d) Y. Lu, C.-Z. Zhao, R. Zhang, H. Yuan, L.-P. Hou, Z.-H. Fu, X. Chen, J.-Q. Huang, Q. Zhang, *Sci. Adv.* **2021**, 7, eabi5520; e) Y. Lu, C.-Z. Zhao, J.-K. Hu, S. Sun, H. Yuan, Z.-H. Fu, X. Chen, J.-Q. Huang, M. Ouyang, Q. Zhang, *Sci. Adv.* **2022**, 8, eadd0510.

[18] a) K. He, C. Wang, Y. He, J. Su, X. Chen, *Chem. Rev.* **2023**, 123, 13796; b) K. He, P. Cai, S. Ji, Z. Tang, Z. Fang, W. Li, J. Yu, J. Su, Y. Luo, F. Zhang, *Adv. Mater.* **2023**, 2311255.

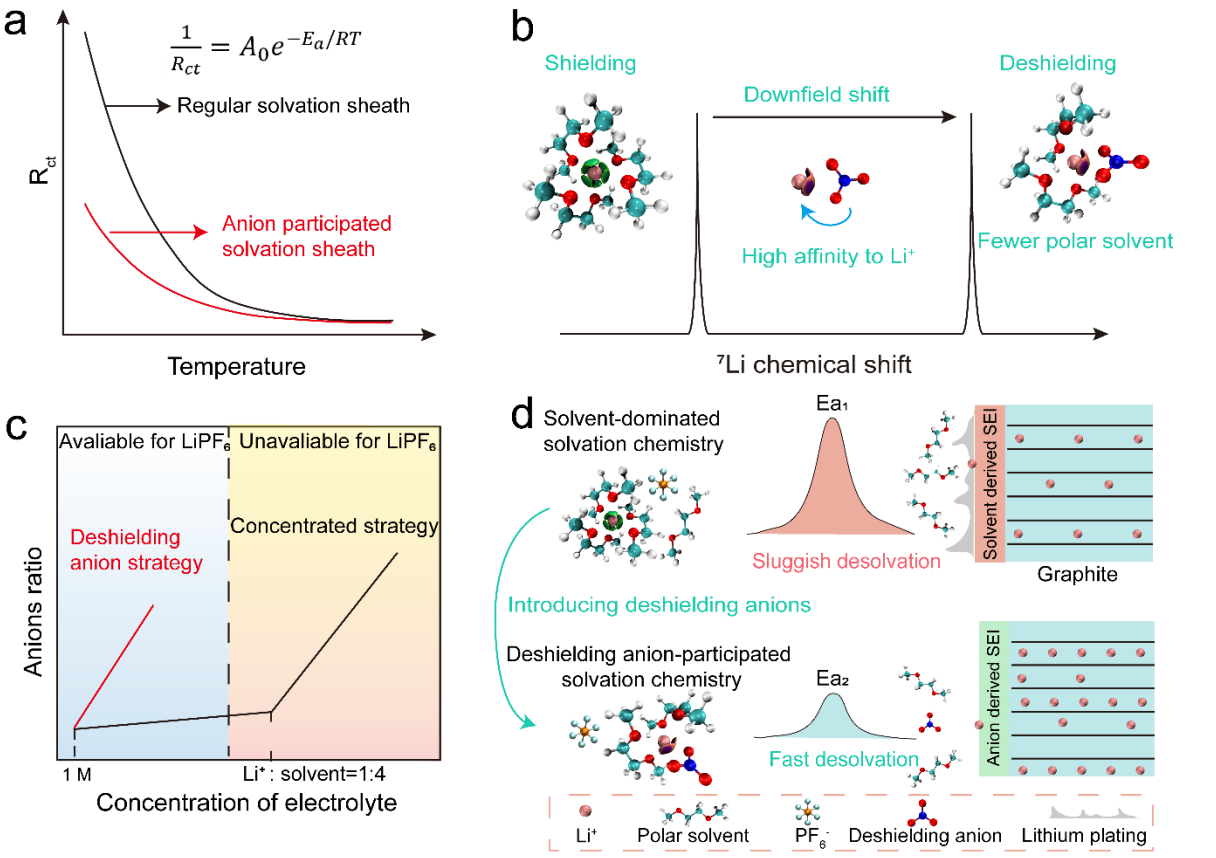

Figure 1. The proposed strategy for $LiPF_6$-based electrolyte design towards low-temperature LIBs. a) The effect of solvation sheath design on the change of R_{ct} with temperature decrease. b) The influence of deshielding anions on solvation structures of lithium ions. The deshielding effect is measured by the peak shift in NMR tests, where a downfield shift indicates the shielding effect of solvents around Li^+ is weakened and Li^+ can feel a stronger magnetic field during the NMR experiment. c) The comparison between the concentrated strategy and the deshielding anion strategy to achieve a high anion ratio in electrolytes. The dashed line represents the maximum concentration of $LiPF_6$-based electrolyte. d) Schematic of the intercalation process for graphite anode in electrolytes with and without the introduction of deshielding anions at low temperatures. The anion participation in the solvation structure will displace part solvents and their desolvation process can be neglected due to a repulsive force applied on them when they move with lithium ions to electrodes.

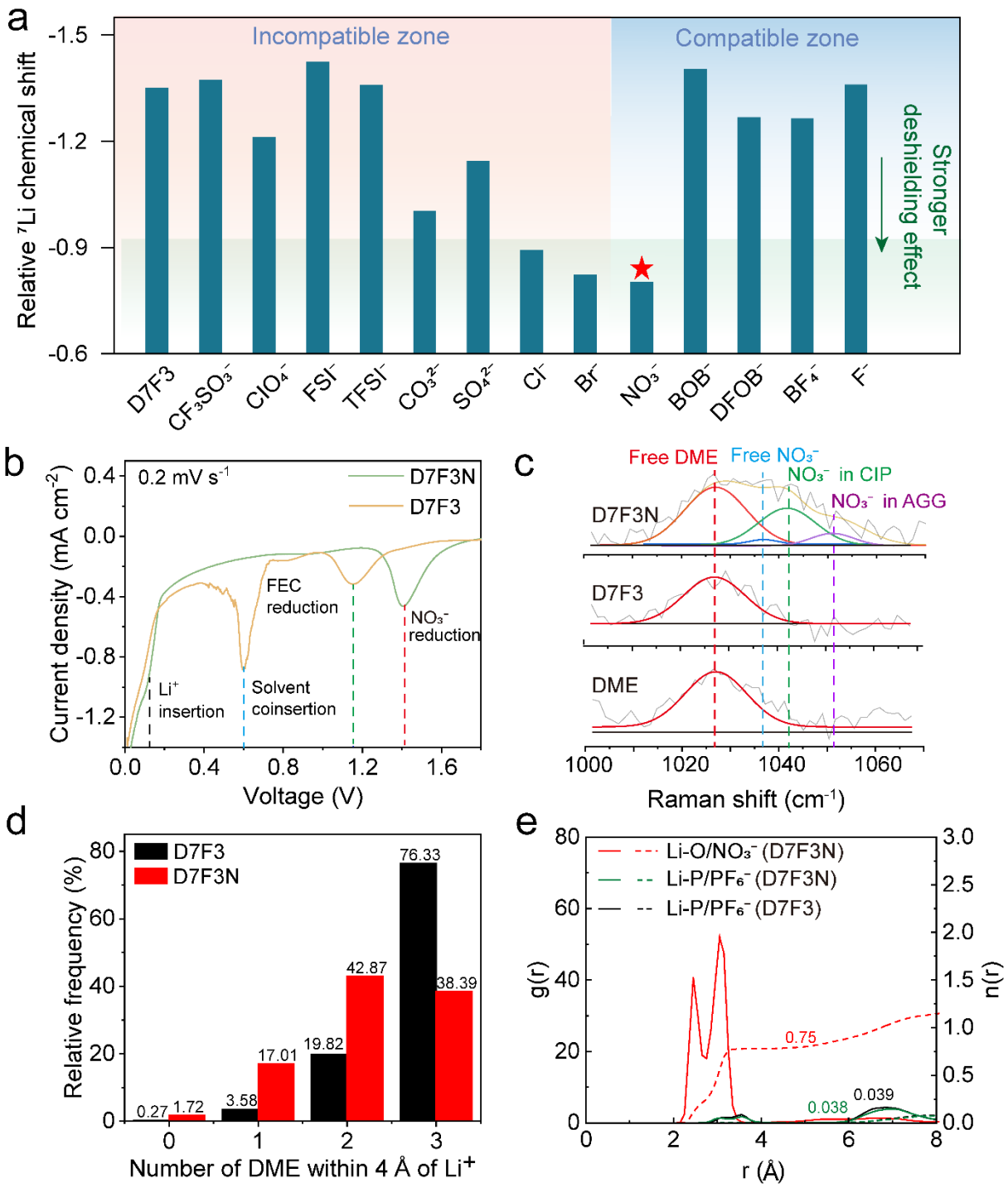

Figure 2. Deshielding anion selection and characterization of electrolyte microstructure. a) The selection of deshielding anions based on the relative ^{7}Li chemical shift and compatibility with graphite anodes. b) The cyclic voltammetry (CV) profiles of graphite/Li cells with D7F3N and D7F3. c) Raman spectra of D7F3N, D7F3 and solvent. d) Coordination number distribution of DME molecules in D7F3 and D7F3N based on the MD simulation results. e) Radial distribution functions of interactions between Li^{+} and anions in the D7F3 and D7F3N.

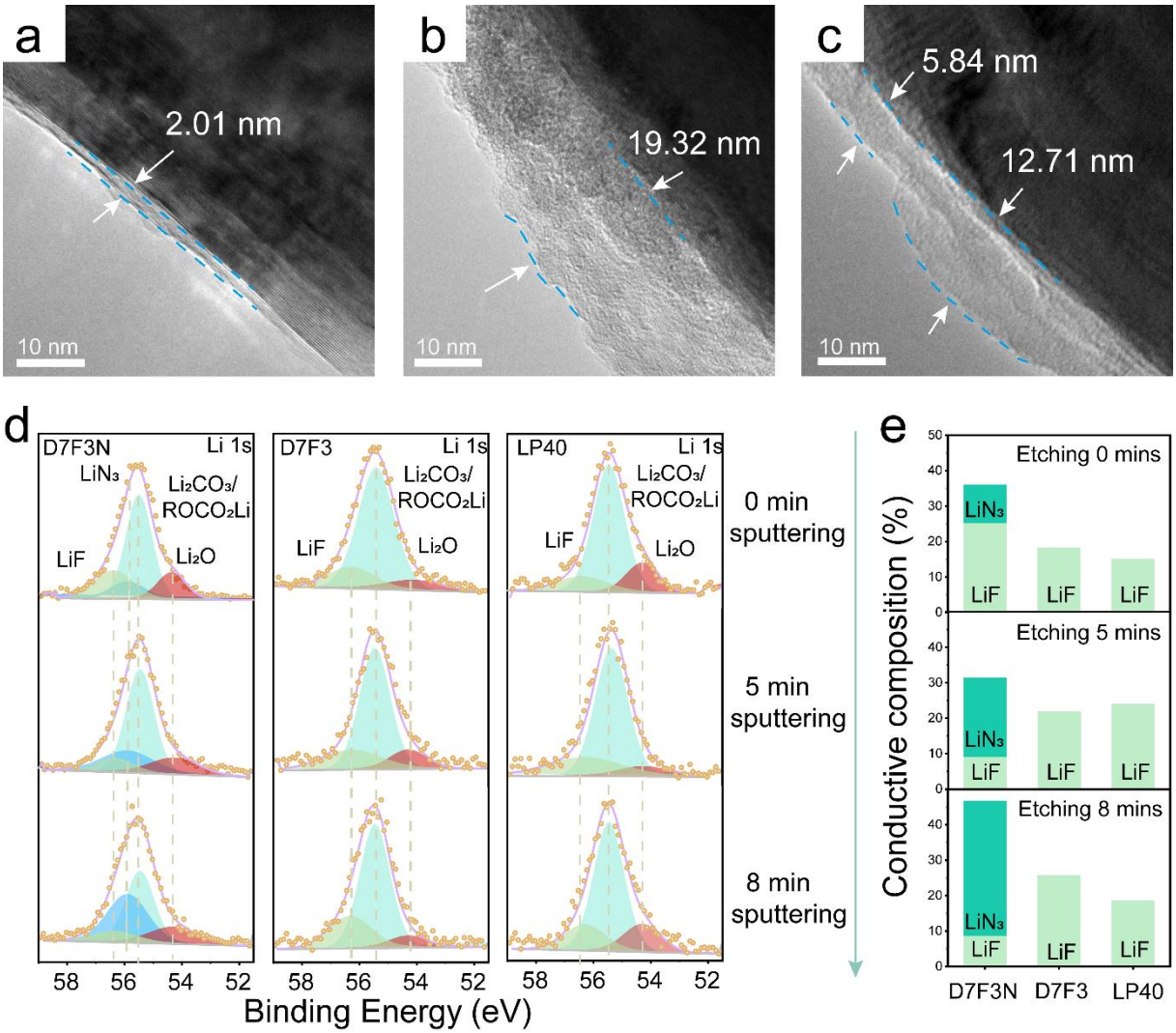

Figure 3. Characterization of the solid electrolyte interfaces (SEI) on graphite anodes in different electrolytes. TEM images of the SEI film on graphite anodes disassembled from the Gr/Li cell in a) D7F3N; b) D7F3 and c) LP40 after ten cycles. d) XPS Li 1s depth profiles of graphite anode in D7F3N, D7F3 and LP40 electrolytes. e) The conductive component content retrieved from d in three electrolytes.

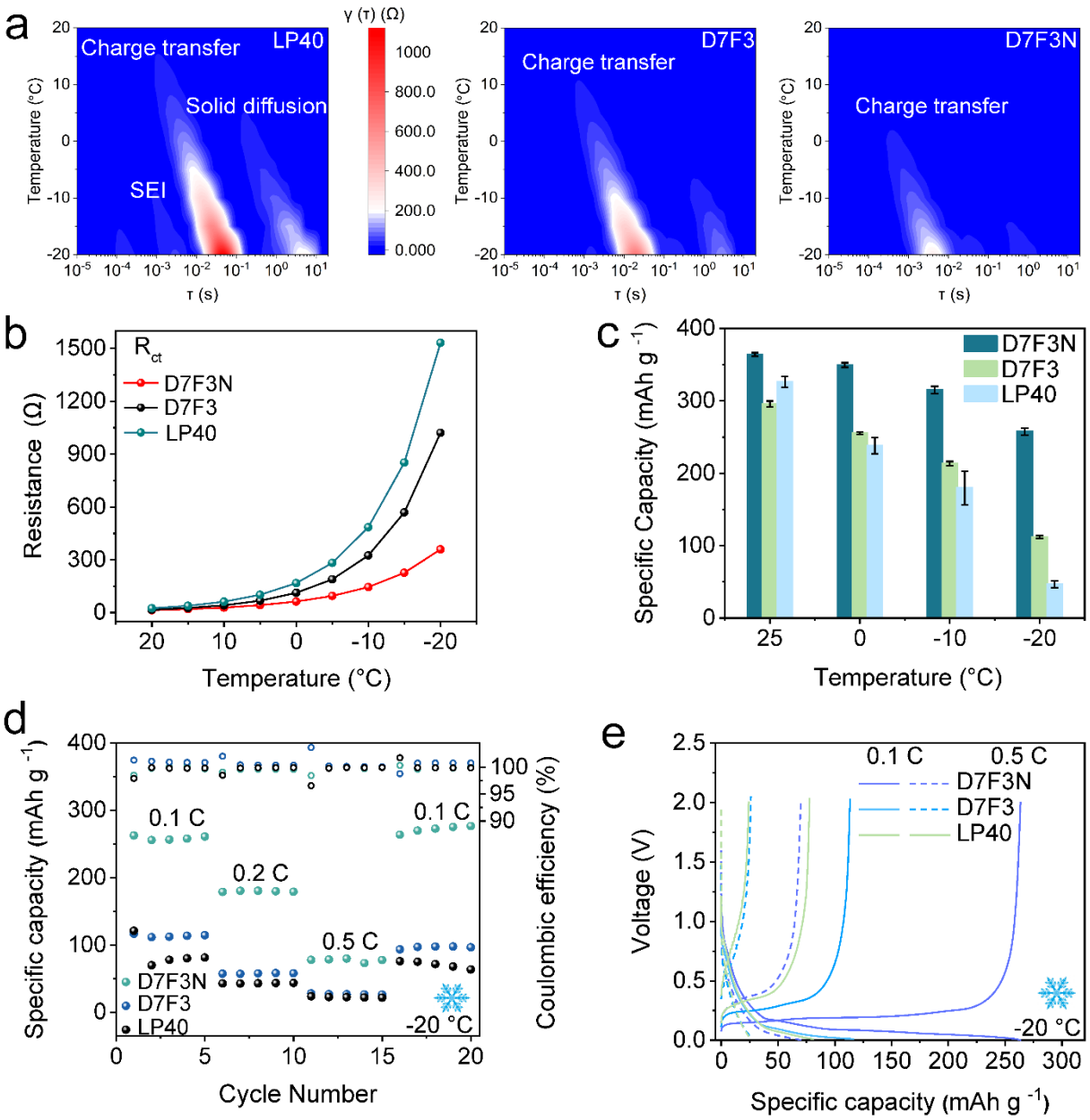

Figure 4. Interfacial kinetics measurement and electrochemical performance of graphite anodes at subzero temperatures. a) DRT analysis of the preprocessed EIS data for the graphite anodes at different temperatures in the LP40, D7F3 and D7F3N. b) The change of R_{ct} with temperature decrease in three electrolytes. c) The capacity retention of graphite anodes at various temperatures. d) Rate capability under −20 °C. e) Voltage curves of 0.1 C and 0.5 C at −20 °C.

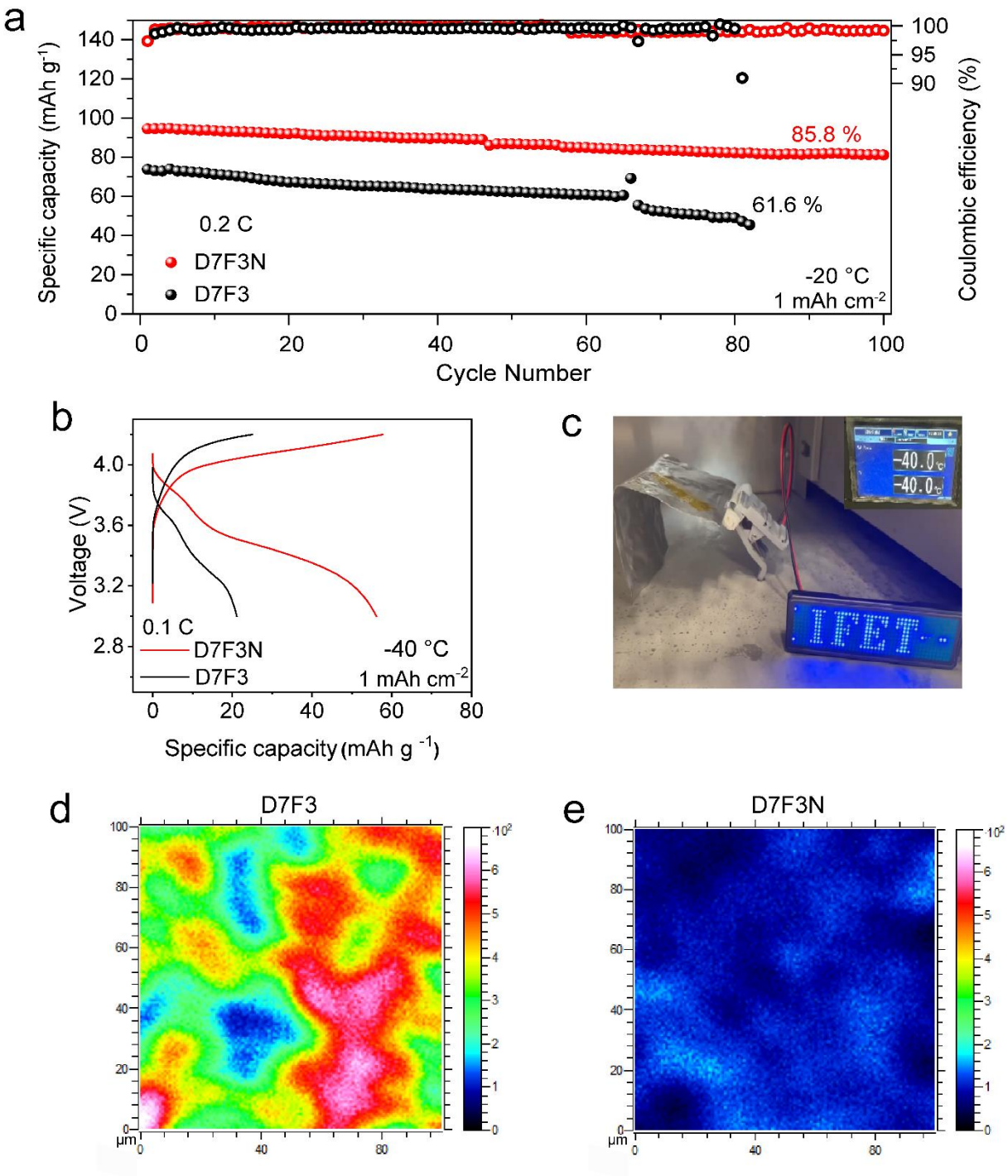

Figure 5. Full cell electrochemical performance test and lithium plating characterization. a) Long-cycling performance of LCO/Gr full cells with 0.2 C at −20 °C in D7F3N and D7F3. b) Voltage curves of 0.1 C at −40 °C. c) Optical images of LED powered by flexible pouch cell with D7F3N operating at −40 °C. Li^- mapping of the graphite anode disassembled from cycled LCO/Gr full cells by TOF-SIMS in d) D7F3 and e) D7F3N.

The table of contents entry

The dilemma of solvation chemistry control for $LiPF_6$-based low-temperature electrolytes can be solved by introducing deshielding anions. As a proof-of-concept, the NO_3^- is selected and the graphite anodes exhibit a higher capacity retention of ≈ 72.3% at −20 ℃ than the counterpart electrolyte (32.3%). The introduced deshielding anions bypass the solubility limitation of $LiPF_6$ and enable the electrolyte based on this most commonly used lithium salt to work under extreme conditions.

Keywords: Deshielding anions, $LiPF_6$-based electrolyte, Solvation design, Low temperature, Lithium-ion batteries.

Deshielding Anions Enable Solvation Chemistry Control of $LiPF_6$-based Electrolyte towards Low-Temperature Lithium-ion Batteries

Song Yuan, Shengkai Cao, Xi Chen, Jiaqi Wei, Zhisheng Lv, Huarong Xia, Jiaofu Li, Hang Zhang, Lin Liu, Changhao Tian, Lixun Chen, Wei Zhang, Zhenxiang Xing, Haicheng Li, Shuzhou Li, Qiang Zhu, Xue Feng* and Xiaodong Chen**

TOC Figure